Materials Today Communications 38 (2024) 107932

Contents lists available at ScienceDirect

Materials Today Communications

journal homepage: www.elsevier.com/locate/mtcomm

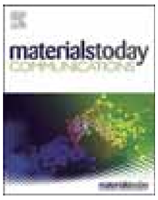

Nickel content-dependent microstructure and mechanical properties of TiZrNbHfNi high entropy alloy thin films

Feng Qin [a,b], Kaiqing Dai [a,b], Shaohua Chen [c], Jianjun Li [a,b,*]

[a] College of Mechanical and Electrical Engineering, Central South University, Changsha 410083, Hunan, PR China
[b] State Key Laboratory of Precision Manufacturing for Extreme Service Performance, Central South University, Changsha 410083, Hunan, PR China
[c] Institute of Advanced Structure Technology, Beijing Institute of Technology, Beijing 100081, PR China

ARTICLE INFO

Keywords:
High entropy alloy film
Composition design
Amorphous structure
Hardness

ABSTRACT

Alloying is known as an effective strategy to improve the mechanical properties of metallic materials. Here we show that the microstructure and mechanical behavior of a $TiZrNbHf_{1.6}$ high entropy alloy film can be highly tuned by Ni addition. The newly designed $TiZrNbHf_{1.6}Ni_x$ ($x = 0, 0.4, 1.2, 1.8, 2.5, 3.0, 4.6$) alloy films are synthesized by co-sputtering Ti, Zr, Nb, Hf and Ni elemental targets. The microstructure and mechanical behavior of the alloy films are investigated by X-ray diffraction (XRD), transmission electron microscopy (TEM), and nano/micro-indentations. The microstructural analysis indicates that the $TiZrNbHf_{1.6}$ film has a single body-centered cubic with columnar-nanograined structure. As Ni content increases to 0.4 or above, the films show a complete amorphous structure. Our theoretical analysis shows that the transition from the crystalline to the amorphous structure can be attributed to the large atomic radius difference and the change of the thermodynamic parameters (e.g., mixing entropy and mixing enthalpy) due to the Ni addition. Compared to the $TiZrNbHf_{1.6}$ film with a hardness of 4.8 GPa, a hardness increase of 8–35% is achieved in the Ni-doped alloy films (5.2–6.5 GPa) as measured by nanoindentation. The elevated hardness may be attributed to the severe lattice distortion and the amorphous structure induced by the Ni addition. Furthermore, microindentation reveals a diversity of deformation behavior in those films with different Ni content. A homogeneous deformation (slight plastic pileup) occurred in the films with Ni content of 1.2 and 4.6, which is close to the deformation behavior of the crystal $TiZrNbHf_{1.6}$ film. While the film with a Ni content of 1.8 exhibits a catastrophic cracking deformation. Finally, multiple shear banding dominates the deformation of these films with Ni content of 0.4, 2.5 and 3.0. Our findings demonstrate that ultrastrong and highly deformable amorphous high entropy alloy thin films can be developed by appropriate element addition, making them promising materials for corrosion and wear-resistant coatings.

1. Introduction

In nearly two decades, high entropy alloys (HEAs) have attracted great scientific attention due to their huge alloy design space and outstanding mechanical properties, such as excellent strength and ductility combinations [1–3], high fracture toughness under cryogenic conditions [4], high corrosion and wear resistances [5]. Unlike the traditional alloying strategy by adding relatively small amounts of secondary elements to improve mechanical properties (e.g., aluminum alloy, titanium alloy, nickel alloy) [6], HEAs are defined as a new class of alloys composed of five or more elements in equiatomic or near equiatomic concentrations (ranging in 5–35%), as proposed by Yeh [7] and Cantor et al. [8] in 2004. The configurational entropy of the HEA system is maximized, which stabilizes solid-solution-like phases with relatively simple crystal structures with face center cubic (FCC) or body center cubic (BCC) solid solution phases and even amorphous structures rather than forming the conventionally expected complex intermetallic phases [9].

The earlier research about HEAs mainly emphasizes alloys based on late-transition metals such as Fe, Ni, Cr, Co and Cu, which are capable of structural function with high strength and high plasticity [10,11]. The tension or compression strength of those HEAs usually reached more

---

* Correspondence to: College of Mechanical and Electrical Engineering and State Key Laboratory of Precision Manufacturing for Extreme Service Performance, Central South University, Changsha 410083, Hunan, PR China.

E-mail addresses: jianjunli.mech@hotmail.com, mejjli@csu.edu.cn (J. Li).

https://doi.org/10.1016/j.mtcomm.2023.107932
Received 11 October 2023; Received in revised form 3 December 2023; Accepted 19 December 2023

than 1 GPa, the uniform elongation of those HEAs is as high as 30–60%, and the compression failure strain also reached 25–33% [12,13]. However, similar to conventional alloys, a rapid decrease in strength of those HEAs occurs at elevated temperatures above ~ 0.6 T_m, where T_m is the melting temperature. For instance, the tensile strength of the CoCrFeNi-based FCC HEAs showed a rapid decrease from ~ 1 GPa to nearly 100 MPa as the temperature increased from − 200 ℃ to 1000 ℃ [10,14], which is far below the application requirements in high-temperature scenarios.

Since Senkov et al. [15] first reported the refractory HEAs (RHEAs, also called Senkov alloys), which can be used in high-temperature load-bearing structures and thermal protection for the aerospace industry, there has been tremendous attention focused on RHEAs due to their ability to retain high strength even up to 1600 °C [16,17]. Generally, the group of RHEAs is composed of the ten metals Ti, Zr, Hf, V, Nb, Ta, Cr, Mo, W and Re. These metals have high melting even beyond 1800 ℃ [18]. For RHEAs, the high strengths displayed, at high temperatures in particular, are very attractive because they surpass state-of-the-art Ni-based superalloys in some cases which are limited by their solvus and melting temperatures and often lose strength at temperatures above 1200 °C [17,19]. However, the significant weakness for most RHEAs is their low ductility at room temperature (RT) and low temperature (< 600 ℃) [15,16,20–23]. For example, NbMoTaW and NbMoTaWV bulk RHEAs only process a compression fracture strain of 2.6% and 1.7%, respectively [16] at RT. Interestingly, among the reported RHEAs, HfNbTiZr [24], HfNbTaTiZr [20] and their derived alloys show RT tensile ductility well in excess of 10% and compressive ductility greater than 50%. However, the yield strength of these TiZrNbHf or TiZrNbHfTa RHEAs is limited (below 1 GPa) compared with other RHEAs (e.g., the group of NbMoTaW RHEAs with yield strength beyond 1 GPa [16]). Therefore, to further elevate the strength/hardness of the group of TiZrNbHf RHEAs is scientifically important and beneficial to engineering applications (e.g, wear-resistant coatings), whereas relevant studies are few and mainly focus on the influence of low melting elements (like Al) on the ductility and high-temperature properties of the bulk RHEAs [17,25,26].

Alloying is a typical strategy to modify the mechanical properties of a material by choosing an appropriate element addition. In principle, the microstructure varies when the component concentration changes in an alloy system due to the differences in physical characteristics among different elements (e.g., atomic size, elastic modulus, valence electron concentration, etc.) [27,28]. For example, by co-sputtering In and CoCrCuFeNi targets, Braeckman et al. [29] observed a transition from FCC structure to an amorphous one as the In content exceeds 8.6 at.%. Also, the group of Hsueh [30–32] reported that the addition of Ti, V, and Nb elements to CoCrFeMnNi films can induce a phase transition from FCC to an amorphous structure, and the hardness of the alloy films increased simultaneously. The elevated hardness/strength in the aforementioned FCC HEA films with element addition [30–32] might be attributed to the high and ubiquitous local lattice distortions produced by neighbor atoms with different atomic sizes [9]. Additionally, by using an uniaxial tensile test combined with density functional theory calculation, Sohn et al. [33] directly proved that the inherent severe lattice distortions in FCC VCoNi bulk HEA can substantially improve the lattice friction stress to eventually realize a high yield strength of ~ 1 GPa in this alloy.

The above studies share a pertinent design strategy for developing alloys with high strength, i.e., inducing severe lattice distortions. Motivated by this paradigm, the nickel (Ni) element is selected to be the alloying element adding in a $TiZrNbHf_{1.6}$ alloy since the atomic radius and modulus of Ni have a large difference from the matrix elements (Ti, Zr, Nb, Hf), which potentially enables a huge space for microstructural regulation and high lattice distortion for strengthening. Here a Hf rich composition ($TiZrNbHf_{1.6}$) is selected as a starting point of the studied alloy films based on the following considerations: (i) the addition of subgroup IV elements (Hf, Ti, Zr) generally improve the toughness of the refractory HEAs [17]. For example, the fracture toughness of the $Hf_{30}Nb_{25}Ta_{25}Ti_{15}Mo_5$ is reached as high as 94.7 ± 1.4 MPa $m^{1/2}$, which is 20% higher than that of the $(TiZrNbTa)_{95}Mo_5$ [34]; (ii) Hf element is extremely corrosion resistant due to the strong oxygen affinity. Therefore, a Hf rich composition may potentially enhance the deformability and the corrosion resistance of the $TiZrNbHf_{1.6}Ni_x$ HEA films.

This study aims to investigate the effect of Ni addition on the microstructure and mechanical properties of the $TiZrNbHf_{1.6}$ HEA thin films. Firstly, a series of $TiZrNbHf_{1.6}Ni_x$ ($x = 0$, 0.4, 1.2, 1.8, 2.5, 3.0, 4.6) HEA films were fabricated by using a magnetron co-sputtering method. The chemic composition, crystallographic structure, mechanical properties including hardness and elastic modulus, and deformation behaviors of the as-prepared HEA films were examined in detail by scanning electron microscopy (SEM), XRD, TEM and nano/micro-indentations. Furthermore, the effect of Ni addition on the phase formation of the HEA films was analyzed based on the calculated thermodynamic parameters, e.g., mixing entropy and mixing enthalpy. Moreover, the correlation between the microstructure and the plastic deformation behaviors was discussed.

2. Materials and methods

2.1. Alloy film preparation

A series of $TiZrNbHf_{1.6}Ni_x$ ($x = 0$, 0.4, 1.2, 1.8, 2.5, 3.0, 4.6) HEA films were synthesized by co-sputtering five pure targets Ti (purity of 99.999%), Zr (purity of 99.9%), Nb (purity of 99.9%), Hf (purity of 99.9%), and Ni (purity of 99.95%) in a magnetron sputtering system (PTL6S PVD system), as illustrated in Fig. 1a. The substrate is a single crystal Si (100) wafer without any heating or cooling before deposition. The background vacuum of the deposition chamber was less than 5×10^{-5} Pa. The work pressure was 1.4 Pa using high-pure (99.999%) Ar gas. Additionally, the path of sputtered atoms from the target to the substrate is arc-type due to the annular configuration of the chamber (as schematized in Fig. 1a), which may lead to an inhomogeneous distribution of elements arriving at the substrate. Thus, a rotation rate of 30 rpm was set for the substrate to homogenize the composition as well as the thickness of the film [31,35]. The power used for Hf and Ni targets was radio frequency (RF) and for other targets was direct current (DC). Technically, both RF and DC powers can be used to sputter all the five metal targets (Ti, Zr, Nb, Hf and Ni). The usage of DC or RF power depends on their specific number in the sputter instrument, which will not alter the microstructure and mechanical properties of the sputtered film. The atomic molar ratio of Ti, Zr, Nb, Hf is designed to be constant, i.e., 1:1:1:1.6, while the content of Ni is increased in proportion by adjusting the power (Table 1). Note that the powers of the other four targets (Ti, Zr, Nb and Hf) in the samples with $x \geq 1.8$ were reduced to obtain the designed Ni content in all the samples without exceeding the power limit (180 W). All samples shared an equivalent total thickness of ~ 1 μm by controlling the deposition time as presented in Table 1. Besides, the as-deposited sample would be heated at a low temperature during the deposition process because the sputtered atoms that possess high kinetic energy would collide with each other during the deposition process, resulting in an increased temperature (~ 350 K) in the sample and the substrate. Therefore, all films were naturally cooled in the vacuum chamber for 2 h after deposition to make the full diffusion of the deposited atoms and avoid delaminating and breaking from the substrate due to internal stress.

2.2. Microstructural characterization

Crystallographic structures of the as-prepared films were identified using XRD (Bruker D8 Advance) with Cu Kα (λ = 0.15406 nm) radiation, and the scanning angle is 2θ ranging from 20–60°. The chemical compositions and uniformity of the as-prepared samples were investigated using energy dispersive X-ray spectroscopy (EDS) with 20 kV in

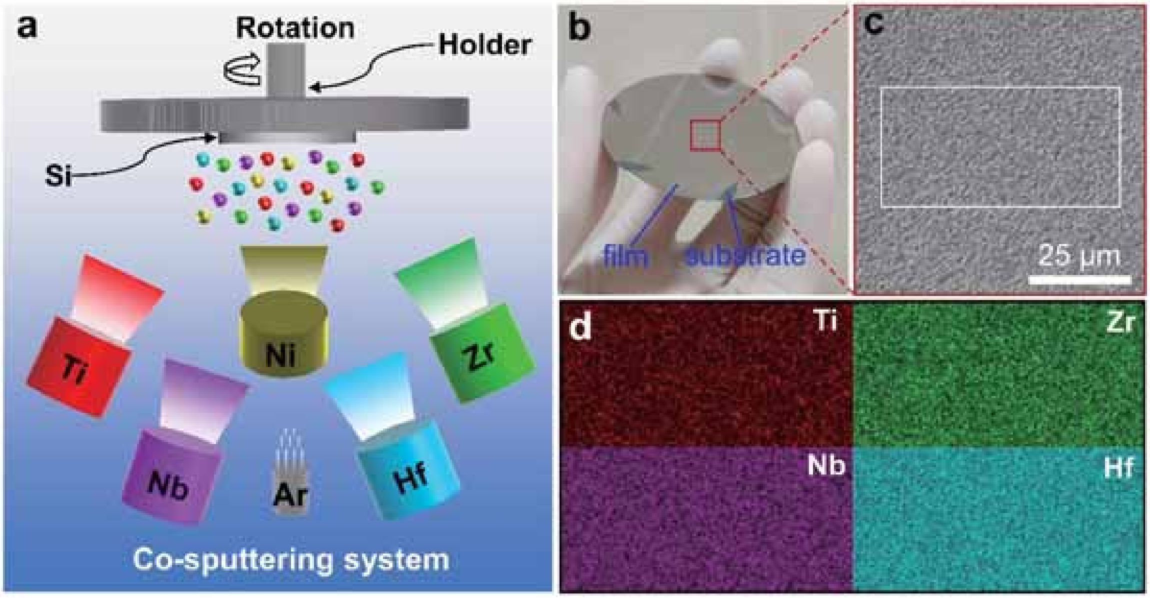

Fig. 1. (a) Schematic diagram of the co-sputtering system used to fabricate the HEA films. (b) Display of the as-prepared sample grown on Si substrate. (c) Surface SEM morphology of the as-deposited $TiZrNbHf_{1.6}$ film. (d) Element mappings of the white rectangular box area indicated in (c).

Table 1
The co-deposition parameters for preparing the $TiZrNbHf_{1.6}Ni_x$ HEA films.

Sample	Power (W)					Deposition time (minute)
	Ti	Zr	Nb	Hf	Ni	
$x = 0$	140	94	90	106	0	44
$x = 0.4$	140	94	90	106	46	42
$x = 1.2$	140	94	90	106	136	39
$x = 1.8$	100	67	64	76	146	51
$x = 2.4$	80	54	51	61	162	60
$x = 3.0$	70	47	45	60	171	65
$x = 4.6$	45	30	29	34	168	90

scanning electron microscopy (SEM, TESCAN MIRA3). The cross-sectional TEM lamellas were prepared using the focused ion beam (FIB) (FEI, Helios Nanolab 600i, and Helios 5CX) milling. Before FIB milling, a 2 μm thick platinum layer was deposited on the sample to prevent ion beam damage. The final milling voltage and the current were 5 kV and 18 pA, respectively, which was small enough to reduce the FIB damage. Subsequently, the cross-sectional micrographs of the RHEA films, including bright-field TEM, selected area electron diffraction (SAED), high-resolution TEM (HRTEM), high-angle annular dark field (HAADF)-scanning TEM (HAADF-STEM) and STEM-EDS mappings were taken in a spherical aberration-corrected FEI Titan Themis microscopy (Titan G2 60–300) operated at 300 kV.

2.3. Nanoindentation and microindentation tests

Nanoindentation (Agilent G200, Berkovich indenter with a radius of 50 nm) tests were used to measure the hardness and elastic modulus. The continuous stiffness measurement (CSM) mode [36] with a constant strain rate of 0.05 s^{-1} was applied. The maximum indentation depth was 350 nm. A total of ten independent tests were performed for each sample to ensure statistical reliability. The deformation of the HEA films was examined using the microindentation (Shimadzu HMV-G20ST) equipped with Vickers indenter with a radius of ~ 14.7 μm. Six microindentation tests, a load of 500 mN with 5 s dwelling time, were conducted on each sample. Subsequently, the deformation morphology induced by microindentation was characterized by SEM (TESCAN MIRA3), and the profile of the residual indents was characterized in an atomic force microscope (Agilent 5500AFM/SPM).

3. Results and discussion

3.1. Microstructures of the as-deposited films

Fig. 1b presents the as-deposited $TiZrNbHf_{1.6}$ film grown on the Si (100) wafer (Fig. 1b). A smooth and mirror effect can be observed from the sample surface, which indicates a small roughness and good film compactness. The surface SEM image (Fig. 1c) of the $TiZrNbHf_{1.6}$ film reveals a nano-needles-like morphology, similar to the surface morphology reported in $W_{5.92}Ta_{89.97}Cr_{1.24}Fe_{1.31}Ni_{1.56}$ HEA film [37]. The corresponding EDS mappings (Fig. 1d) demonstrate the uniformity of the constituent elements without obvious clusters. Fig. 2 shows the surface morphology of the as-prepared $TiZrNbHf_{1.6}Ni_x$ HEA films with different Ni content. It can be seen that the microstructure of the film surface does not vary significantly with changing the composition even the Ni content increased to 38.5 at.% ($x = 3.0$). However, a smooth surface morphology accompanied by a large number of nano-cracks occurs in the alloy film with a Ni content of 50.8 at.% ($x = 4.6$) (Fig. 2f). Also, nano-cracks have also been reported in the as-prepared $W_{15.39}Ta_{38.81}Cr_{14.58}Fe_{15.45}Ni_{15.77}$ HEA film [37]. These nano-cracks may be attributed to the high lattice distortion and stress produced by the large difference in atomic size in the alloy system [33]. Besides, the representative EDS mappings (Fig. 2g) show the homogeneity of the component elements with Ni addition. The chemic concentrations measured by EDS for all samples are presented in Table 2, which confirms the compositions of each sample with different Ni content. The deviation between the actual atomic percentage and the normal one for each element is less than 3%, which is considered as a reasonable deviation range of the co-sputtering deposition.

Fig. 3 presents the XRD patterns of the as-prepared $TiZrNbHf_{1.6}Ni_x$ films. It can be seen that the $TiZrNbHf_{1.6}$ film ($x = 0$) exhibits sharp diffraction peaks, which indicates the instinct crystalline structure. Further analysis confirms that the film has a single BCC structure with typical (110) and (200) textures. As the Ni content increased to 0.4 or above, a broad diffraction hump with low intensity occurs in those films, which indicates a typical characteristic of the amorphous alloys. It can be noted that the intensity of the peak of $x = 3.0$ is relatively low, which is close to that of the $x = 1.8$ and 1.2, whereas that of $x = 1.2$, 2.5 and

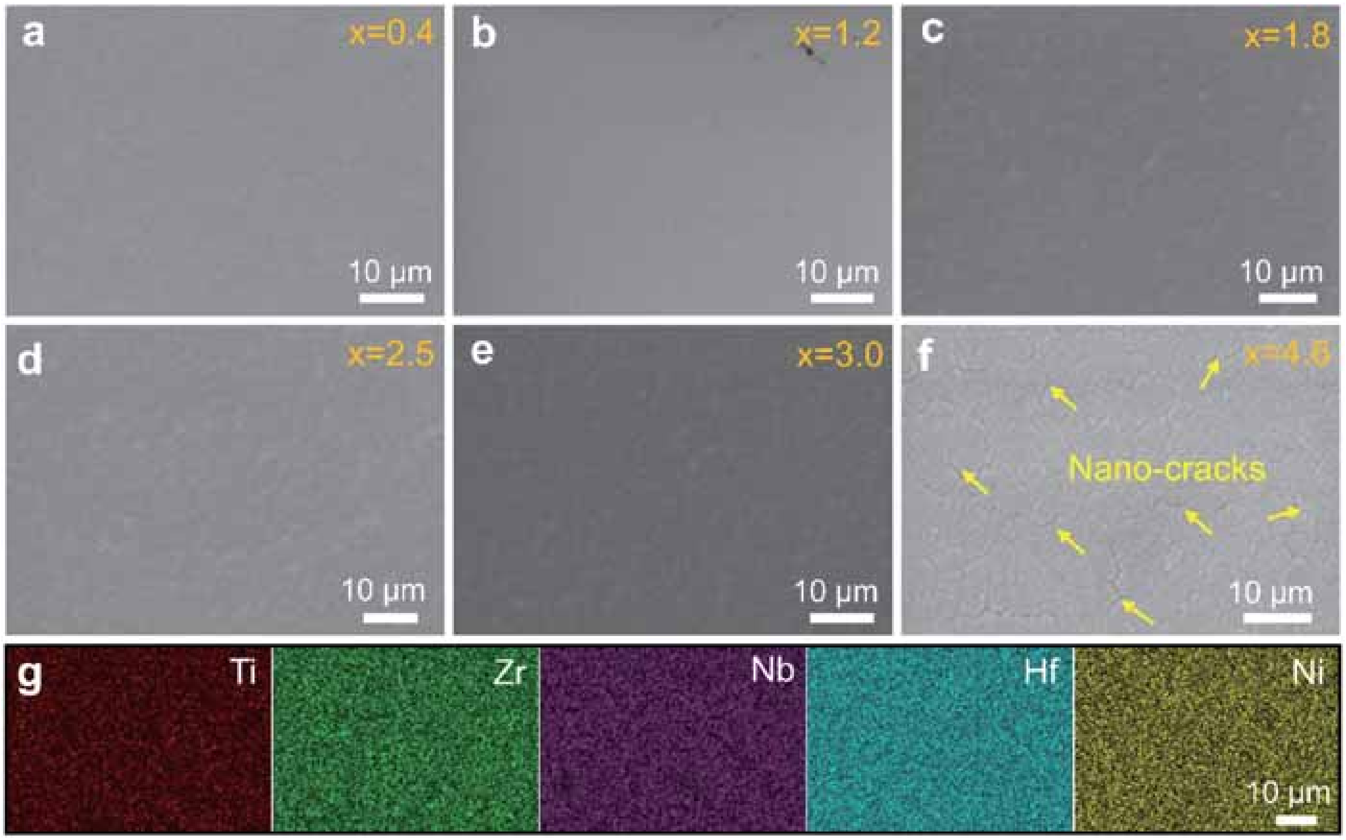

Fig. 2. Surface morphologies of the as-prepared $\mathrm{TiZrNbHf_{1.6}Ni_x}$ HEA films. (a–f) SEM image of $x = 0.4$, 1.2, 1.8, 2.5, 3.0 and 4.6, respectively. (g) Element mappings of (f), i.e., $\mathrm{TiZrNbHf_{1.6}Ni_{4.6}}$ film.

Table 2
The compositions (at.%) of the as-deposited $\mathrm{TiZrNbHf_{1.6}Ni_x}$ samples as measured using the EDS with 20 kV.

Samples	Ti	Zr	Nb	Hf	Ni
$x = 0$	20.5	22.7	22.1	34.7	0
$x = 0.4$	22.8	19.1	19.7	30	8.4
$x = 1.2$	15.3	17.4	16.7	30.2	20.4
$x = 1.8$	16.7	15.1	15.1	24.6	28.5
$x = 2.5$	14.6	13.5	13.1	24.3	34.5
$x = 3.0$	13.9	12.9	12.4	22.3	38.5
$x = 4.6$	10	12.3	7.7	19.2	50.8

4.6 is similar. This difference in the peak shape between these samples may be attributed to the distinct diffraction intensity induced by the composition variation [38]. Besides, the position of the peak for $x = 3$ agrees with the trend of the amorphous peak in the series of $\mathrm{TiZrNbHf_{1.6}Ni_x}$ films, which moves to higher angles with the increase of the Ni content. For example, for $x = 0.4$, $x = 3.0$ and $x = 4.6$, the peak is located at 36.6°, 39.1° and 40.5°, respectively. This deflection of the diffraction peak is indicative of reflections from the increase of Ni element which has a FCC (111) peak at ~ 45°.

The cross-sectional TEM observations of the as-prepared $\mathrm{TiZrNbHf_{1.6}}$ film are presented in Fig. 4. The bright-field TEM image (Fig. 4a) and corresponding SAED pattern (inset in Fig. 4a) reveal a typical polycrystalline structure. Note that the grains are columnar in shape and exhibit the needle geometrical morphology, where the diameter increases gradually from the bottom to the surface. For example, the measured diameter of the columnar grains near the substrate is ~ 35 nm while that of the grains near the sample surface is as high as 150 nm, which indicates that the grain size of the as-deposited $\mathrm{TiZrNbHf_{1.6}}$ film grows gradually with the deposition process. This phenomenon has also been observed in sputtered CrCoFeMnNi HEA films [35]. The HRTEM micrograph (Fig. 4b) and the enlarged microstructure (inset in Fig. 4b) taken along the [111] zone axis reveal the typical BCC lattice arrangement, which is consistent with the XRD results. Furthermore, the corresponding FFT pattern (Fig. 4c) indicates the representative $(1\bar{1}0)$ and $(0\bar{1}1)$ orientations for the BCC lattice. The HAADF-STEM image (Fig. 4d) and corresponding EDS mappings (Fig. 4e) further display the columnar-grained microstructure of the $\mathrm{TiZrNbHf_{1.6}}$ film, where a

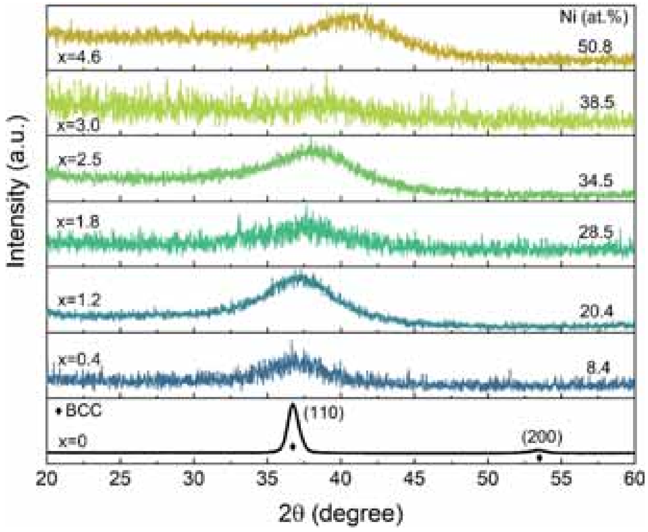

Fig. 3. X-ray diffraction (XRD) patterns of the $\mathrm{TiZrNbHf_{1.6}Ni_x}$ ($x = 0$, 0.4, 1.2, 1.8, 2.5, 3.0, 4.6) HEA films.

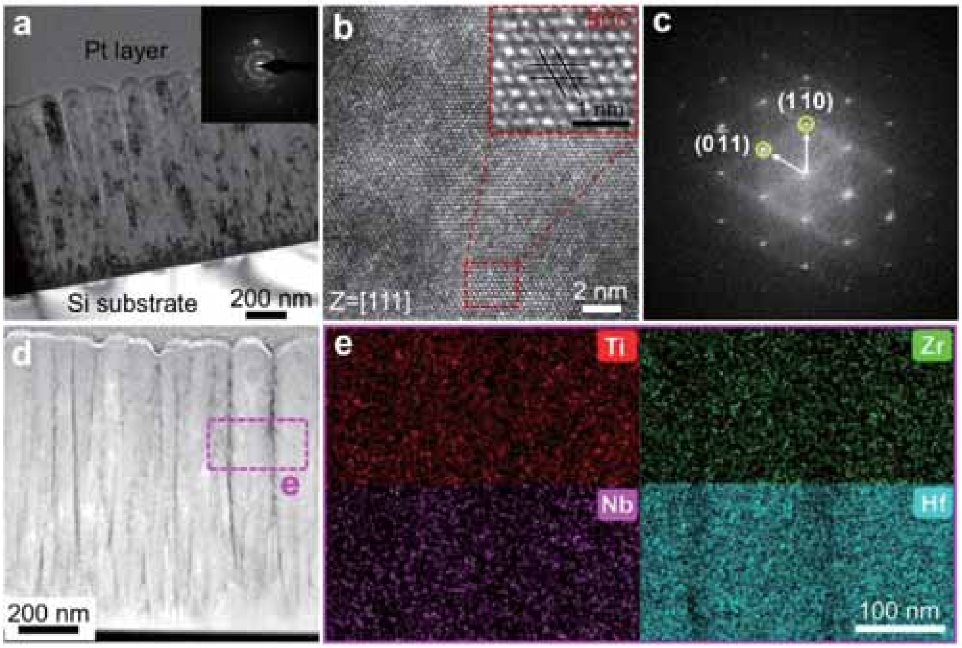

Fig. 4. Microstructures of the TiZrNbHf$_{1.6}$ HEA film. (a) Cross-sectional bright-field TEM image. (b) HRTEM micrograph taken along the [111] zone axis, the inset in (b) shows the typical BCC lattice arrangement. (c) The fast Fourier transform (FFT) pattern of (b). (d) Cross-sectional HAADF-STEM image, indicating the columnar grains of the sputtered TiZrNbHf$_{1.6}$ film. (e) EDS mappings of the box region indicated in (d).

deficiency of elements at the columnar boundary can be detected (Fig. 4e). This phenomenon of element deficiency at the columnar boundary observed from the EDS mappings is mainly induced by the special grain morphology of the TiZrNbHf$_{1.6}$ film. The excessive growth of columnar structure in the vertical direction leads to the appearance of ditch-like between the boundaries of the columnar grains structure (Fig. 4d), i.e., shadow effect [39]. Thus, during the process of EDS scanning, the EDS detector will preferentially collect more element information inside the grain than the grain boundary since there exists a plane difference in height between the grain and grain boundary, resulting in a large difference in the bright and dark contrast of the elements between the grain and the grain boundary.

Fig. 5 shows the microstructure of the amorphous HEA films with Ni addition of 8.4 at.% and 34.8 at.%, i.e., TiZrNbHf$_{1.6}$Ni$_{0.4}$ (Fig. 5a–c), TiZrNbHf$_{1.6}$Ni$_{2.5}$ (Fig. 5d–f). First, no obvious crystalline characteristics (e.g., grain boundary) can be detected from the bright-field TEM images for both films (Fig. 5a and d). The corresponding SAED patterns (insets in Fig. 5a and d) show a broad diffraction ring for TiZrNbHf$_{1.6}$Ni$_{0.4}$ and TiZrNbHf$_{1.6}$Ni$_{2.5}$ films, which reveals their amorphous nature. Moreover, an obvious halo ring can be observed from the FFT patterns (insets in Fig. 5b, c, e and f), which further confirms the amorphous structure of Ni-doped HEA films, and this finding is consistent with XRD results. Second, one can see that a high density of bright bands, 1–2 nm wide, form along the growth direction in both amorphous samples, which is clearly indicated by the red arrows in the inset in Fig. 5a. Interestingly, these bright bands seem more prevalent in the internal of the film, while gradually decrease or even disappeared near the sample surface. This phenomenon can be further proved by the HRTEM observations by detecting the region in the internal (A-I, D-I) and those near the surface regions (A-II, D-II) for the two samples. It can be seen that obvious bright bands can be captured in Fig. 5b and e (indicated by bright yellow arrows), whereas no bright bands can be observed in Fig. 5c and f.

This type of bright band might be originated from the β relaxation process of the amorphous alloys. In principle, β relaxation, which is thermally activated and stress-assisted, occurs when undergoing a temperature high enough to trigger β relaxations (~ 310 K [40]). In the present study, considering that the high-energy atomic collision during the co-sputtering process generated a temperature (at least 350 K detected by the temperature detector connected to the substrate, which is higher than the β relaxation temperature (~ 310 K) while lower than the α relaxation temperature (~ 430 K) for amorphous alloys [40]. In particular, the β relaxation corresponds to the local linkage of shear transformation zones (STZs) [41] as illustrated in Fig. 5g, which might be captured in the form of bright bands (or referred as nano shear bands (NSBs)) in the amorphous matrix as the observed microstructures in Fig. 5a. Besides, studies [42,43] have shown that both the fast quenching from the high temperature to RT and the as-deposited form without any heating could produce similar bright bands in the amorphous matrix, whereas the former would reserve higher-density bright bands than the latter. For example, similar bright bands have also been observed in crystalline-layer confined amorphous NiW alloy films with fast quench from high temperature to RT [42], and CuZr amorphous alloys in the as-deposited crystalline Cu/amorphous CuZr layered films without any extra heating [43], both of which were attributed to the β relaxation. Therefore, abundant NSBs could form in the TiZrNbHf$_{1.6}$Ni$_x$ films after deposition due to the activation of β relaxations. In addition, the process from 350 K to RT after deposition needs about 1–2 h, which is considered as a slow annealing process. Then, the formed NSBs would annihilate upon structural relaxation in amorphous alloys when no surface confining [44]. Thus, it is expected that few NSBs can be reserved near the film surface region, whereas high-density NSBs are reserved in the inner of the film due to the fast cooling of the deposition, which is a typical feature of the sputtering deposition. In other words, there is a rapidly quenched effect during the formation of the thin films [37]. It is emphasized that these NSBs (bright bands) are not caused by the segregation of specific elements, which can be supported by the STEM-EDS mappings (Fig. 6), where the five component elements are distributed uniformly without obvious segregation or precipitation.

The above microstructural analysis results demonstrate that the addition of Ni makes the phase structure of TiZrNbHf$_{1.6}$ HEA films transmit from a single BCC to an amorphous structure. According to Zhang et al. [45,46] and Guo et al. [47,48], the formation of a solid solution or amorphous structure can be predicted in terms of atomic size difference (δ) and the thermodynamic parameters Ω, which are defined as follows [46]:

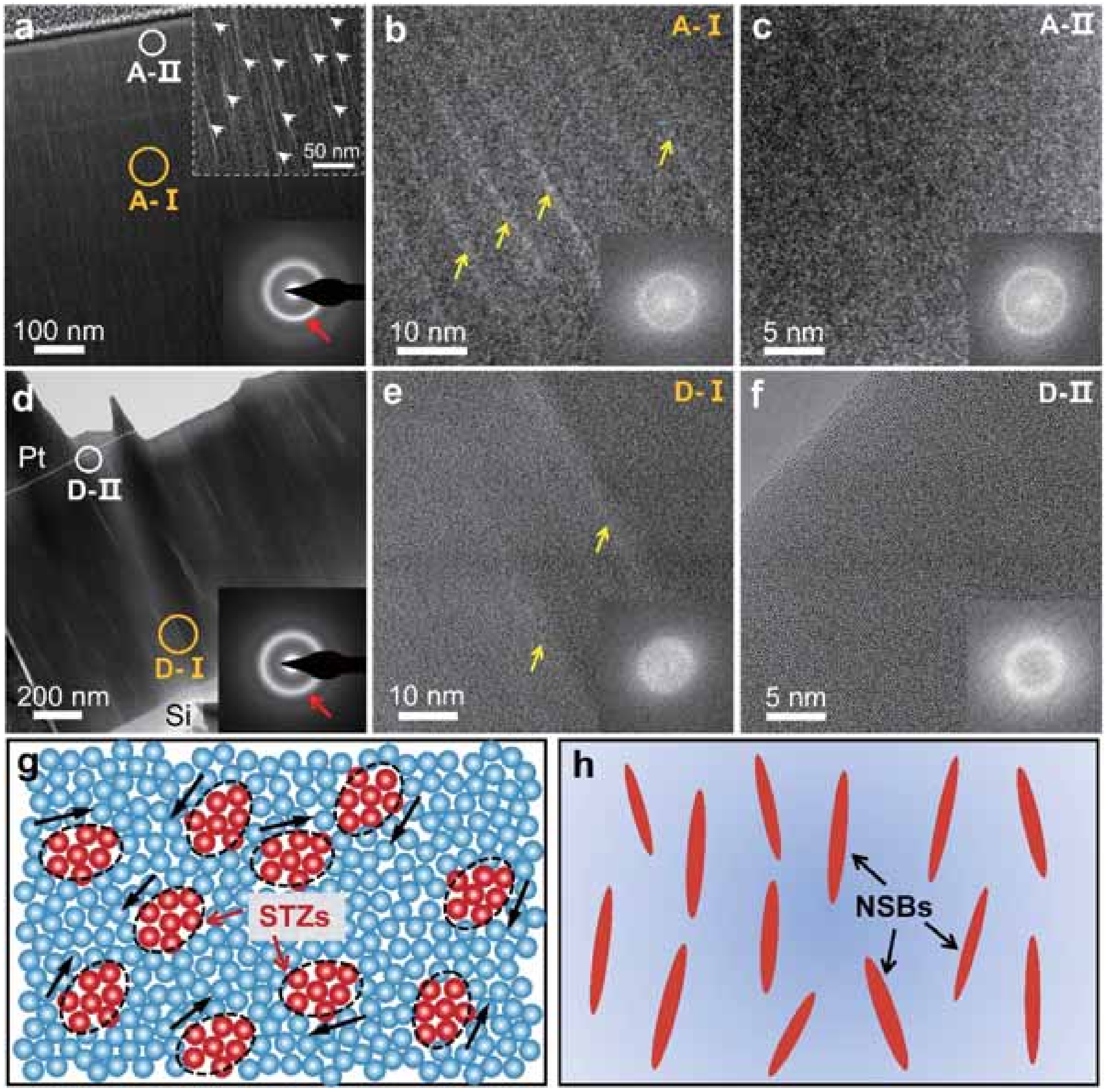

Fig. 5. Cross-sectional TEM microstructures of the amorphous HEA films. (a) and (d) Bright-field TEM images of the as-prepared TiZrNbHf$_{1.6}$Ni$_{0.4}$ (a) and TiZrNbHf$_{1.6}$Ni$_{2.5}$ (d) samples, respectively. The insets in (a) are the SAED pattern and the high magnification of the as-deposited microstructures of TiZrNbHf$_{1.6}$Ni$_{0.4}$ film, while the inset in (d) is the corresponding SAED pattern of TiZrNbHf$_{1.6}$Ni$_{2.5}$ film. (b, c) and (e, f) HRTEM micrographs taken from (a) and (b), respectively. The insets are the corresponding FFT patterns. (g) Schematic diagram of the potentially shear transformation zones (STZs) in the as-deposited amorphous matrix. (h) Illustration of the nano shear bands (NSBs) formed in the amorphous matrix, which is associated with the local linkage of STZs during β relaxation.

$$\delta = \sqrt{\sum_{i=1}^{n} c_i (1 - r_i/\bar{r})^2} \tag{1}$$

$$\Omega = \frac{T_m \Delta S_{mix}}{|\Delta H_{mix}|} \tag{2}$$

where $\bar{r} = \sum_{i=1}^{n} c_i r_i$ is the average atomic radius for the alloy, r_i is the atomic radius of the component, and ΔH_{mix} is the mixing enthalpies of the HEA alloy system with n elements, which can be expressed as [49]:

$$\Delta H_{mix} = \sum_{i=1, i \neq j}^{n} \Delta H_{ij}^{mix} c_i c_j \tag{3}$$

in which $\Delta H_{ij}^{mix} = 4\Delta H_{AB}^{mix}$, ΔH_{AB}^{mix} is the mixing enthalpy of binary liquid alloys and can be obtained in [50], as presented in Table 3. c_i or c_j is the mole percent of each element. ΔS_{mix} is the mixing entropies of an n-element regular solution according to Boltzmann's hypothesis and can be written as follows [7]:

$$\Delta S_{mix} = -R \sum_{i=1}^{n} (c_i \ln c_i) \tag{4}$$

where $\sum_{i=1}^{n} c_i = 1$, $R = 8.314\ \mathrm{JK^{-1}mol^{-1}}$ is gas constant. $T_m = \sum_{i=1}^{n} c_i (T_m)_i$ is the melting temperature. The values of the parameters T_{m} and r_i of each element are listed in Table 4.

As a consequence, the calculated parameters Ω, δ as well as ΔH_{mix}, ΔS_{mix} are presented in Table 5. Yang and Zhang et al. [46] suggested that the HEAs tend to form a solid-solution structure within the range $\Omega \geq 1.1$, $\delta \leq 6.6\%$; while the formation of the amorphous phase is determined by ΔH_{mix} and δ, i.e. $\Delta H_{\mathrm{mix}} \leq -12.2$ kJ/mol, $\delta \geq 6.4\%$ according to Guo et al. [48]. It can be noted that the values of those parameters for BCC structured TiZrNbHf$_{1.6}$ and those Ni-doped amorphous TiZrNbHf$_{1.6}$Ni$_{x}$ (x = 0.4, 1.2, 1.8, 2.5, 3.0, 4.6) films meet the above criteria, which indicates that HEA films could be designed by using the thermodynamic parameters based design criteria for bulk HEAs. To more clearly show the relationship between parameters Ω, δ and the

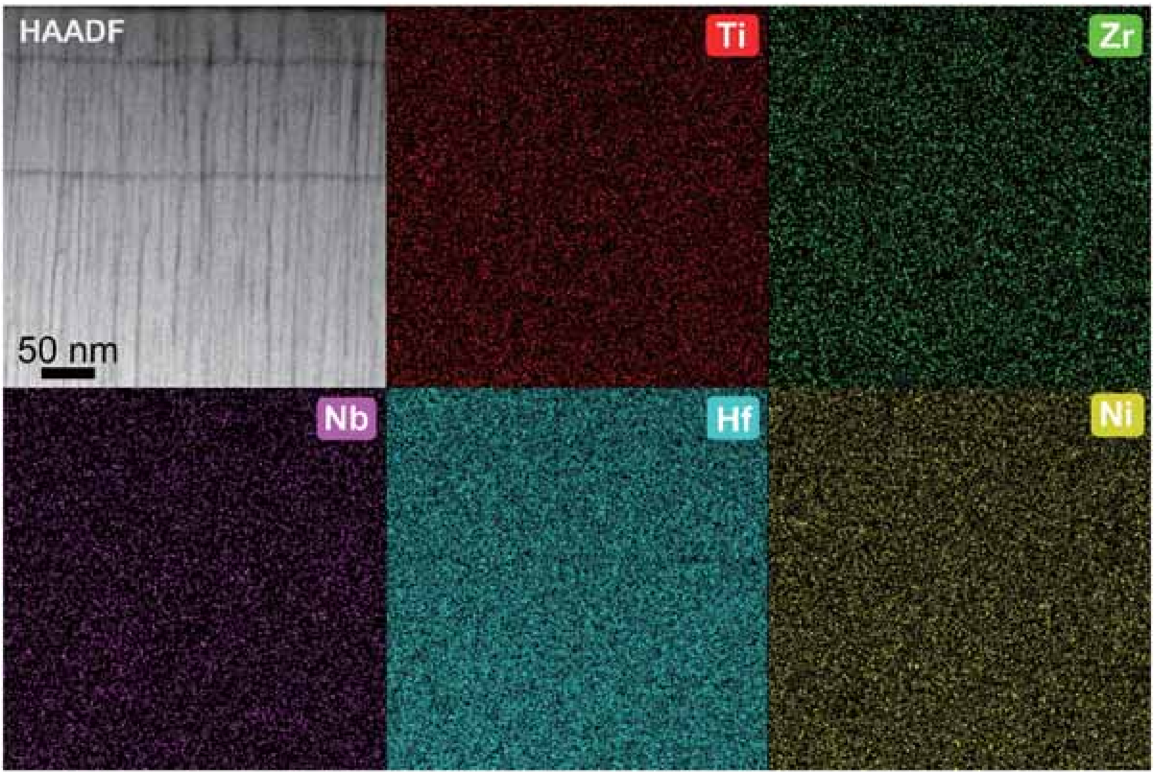

Fig. 6. Representive cross-sectional HAADF-STEM micrograph and corresponding EDS mappings of the as-deposited TiZrNbHf$_{1.6}$Ni$_{0.4}$ HEA film.

Table 3
Mixing enthalpies ΔH_{mix} (kJ•mol^{-1}) of different binary elements [50].

ΔH_{mix}	Ti	Zr	Nb	Hf	Ni
Ti	0	0	2	0	– 35
Zr	0	0	4	0	– 49
Nb	2	4	0	4	– 30
Hf	0	0	4	0	– 42
Ni	– 35	– 49	– 30	– 42	0

Table 4
Melting point, shear modulus and atomic radius of the elements, which are directly adopted from Refs. [47,51,52].

Element	Melting point (K)	Shear modulus (GPa)	Atomic radius (Å)
Ti	1939	44.16	1.462
Zr	2125	35.51	1.603
Nb	2741	37.5	1.429
Hf	2470	55.95	1.578
Ni	1728	76.03	1.246

Table 5
Calculated parameters ΔS_{mix}, ΔH_{mix}, T_m, Ω and δ for TiZrNbHf$_{1.6}$Ni$_x$ RHEA films.

Samples	ΔS_{mix} (J•K^{-1}•mol^{-1})	ΔH_{mix} (kJ•mol^{-1})	T_m (K)	Ω	δ (%)
x = 0	11.33	2.39	2342.72	11.09	4.7
x = 0.4	12.82	– 10.14	2274.1	2.88	8.7
x = 1.2	13.11	– 24.29	2222.62	1.2	8.9
x = 1.8	13.08	– 30.92	2160.62	0.91	9.6
x = 2.5	12.71	– 34.78	2125.41	0.78	10.2
x = 3.0	12.47	– 36.54	2099.62	0.72	10.4
x = 4.6	11.19	– 39.99	2018.4	0.57	11.04

phase structure of the TiZrNiHf$_{1.6}$Ni$_x$ RHEA films, the map of the Ω, δ for the films and those of other reported bulk HEAs are plotted in Fig. 7. First, it clearly shows that Ω is inversely proportional to the Ni content, while δ is proportional to the Ni content (inset in Fig. 7). Second, the crystallographic structure of the TiZrNbHf$_{1.6}$Ni$_x$ films is in good agreement with the phase predicted by the parameters Ω and δ, which are divided to the solid solution region (the blue area) and amorphous region (the orange region). The above theoretical analyses demonstrate that the atomic size difference and the change of thermodynamic conditions induced by Ni addition are the key points that trigger the phase transition of the TiZrNbHf$_{1.6}$Ni$_x$ from a BCC solid solution to an amorphous structure.

3.2. *Mechanical properties*

Nanoindentation tests were performed to measure the hardness and elastic modulus of the TiZrNbHf$_{1.6}$Ni$_x$ RHEA films, as plotted in Fig. 8. It can be seen that the hardness decreases rapidly at first as the depth increases due to the size effect of nanoindentation (Fig. 8a). The hardness reaches a plateau when the penetration depth is reached around 120 nm (~ 10% of the film thickness), and further increases with the increase of the indentation depth when the depth exceeds 200 nm. According to Saha and Nix [65], the effect of the hard substrate on the hardness of the soft film can be ignored since the plastic deformation was contained only in the film at a small indentation depth (below 15% of the sample thickness). Thereby, the plateau in the hardness-displacement curve can be considered as the intrinsic hardness of the films [65]. The elastic modulus of the films decreases rapidly at first as the depth is below 50 nm and increases slowly in the depth of 50–100 nm (Fig. 7b). Subsequently, the elastic modulus shows a rapid increase with the penetrating of the indenter, which can be attributed to the higher stiffness of the Si substrate than the RHEA films [65]. Thus, the elastic modulus of the composites is calculated using the data in the depth of 50–100 nm, in which depths the substrate effect is insignificant. As a consequence, the variation of the hardness (*H*) and elastic modulus (*E*) with Ni content is

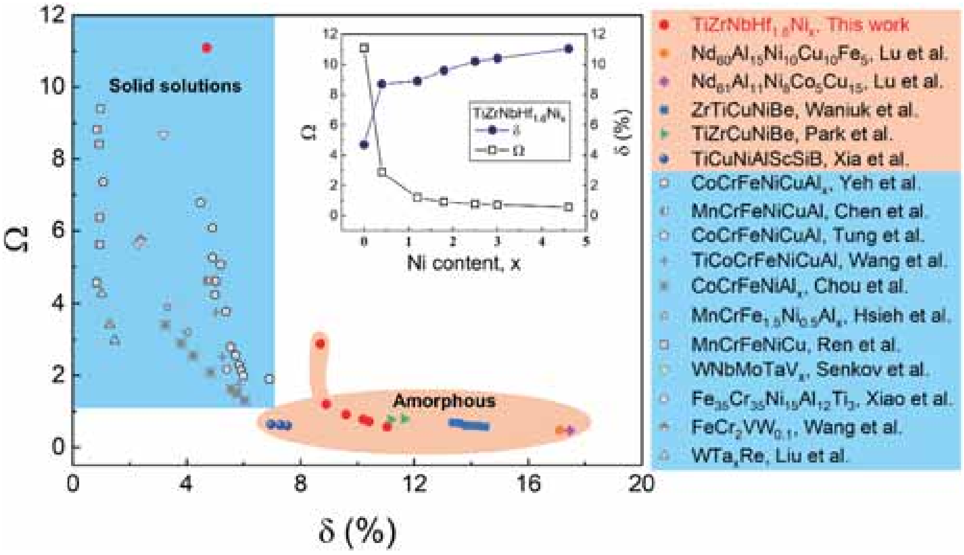

Fig. 7. Relationship between parameters Ω and δ for the $TiZrNbHf_{1.6}Ni_x$ HEA films. The inset is the variation of the Ω and δ with the Ni content. The values of Ω and δ for other reported HEAs [7,15,53–64] are included for comparison. The area in blue indicates the alloy with solid solution structure, while the regions in orange indicate the alloy with an amorphous structure.

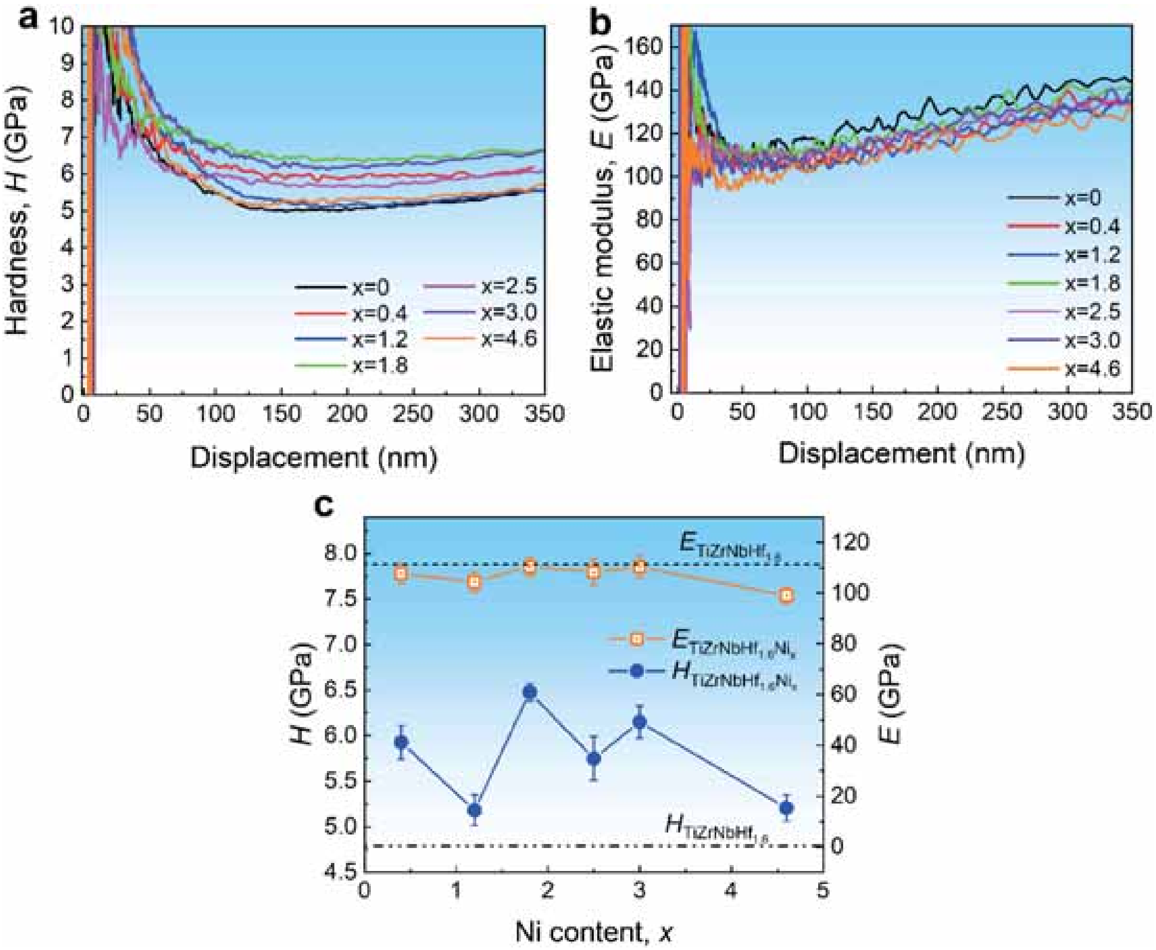

Fig. 8. Representative indentation depth-dependent hardness (a) and elastic modulus (a) curves of the $TiZrNbHf_{1.6}Ni_x$ (x = 0, 0.4, 1.2, 1.8, 2.5, 3.0, 4.6) HEA films. (c) The variation of hardness and elastic modulus with the Ni content.

presented in Fig. 8c. Both hardness and the elastic modulus are obtained by averaging the data from ten independent tests. It clearly shows that the samples with Ni-doped possess a higher hardness than the film without Ni addition. The elevated hardness in Ni-doped alloy films may be attributed to the severe lattice distortion and the amorphous microstructure produced by the large atomic size difference between the base elements Ti, Zr, Nb, Hf and the added element Ni. For instance, the atomic size difference (δ) of the $TiZrNbHf_{1.6}Ni_{0.4}$ system is about twice of the $TiZrNbHf_{1.6}$ system, i.e., 8.7% for the former and 4.7% for the later as presented in Table 5. Besides, the elastic modulus does not change significantly in the films with different Ni content and is slightly lower than that of the BCC-structured $TiZrNbHf_{1.6}$ film.

To evaluate the mechanical properties of the newly designed $TiZrNbHf_{1.6}Ni_x$ RHEA films, the relation of H^3/E^2 and H/E (particularly predicting the wear resistance than the H alone [66]) of the films and the other bulk RHEAs [5,20–22,25,67–69], RHEA films [70] and pure elements [20] are plotted in Fig. 9. The value of H/E denotes an elastic deformation factor, reflecting the ability of the film to resist elastic strain [66]. The value of H^3/E^2 is a plastic deformation factor, reflecting the ability of the material to dissipate energy during plastic deformation [71]. It can be clear from Fig. 9 that both the H/E and H^3/E^2 values of the $TiZrNbHf_{1.6}Ni_x$ RHEA films (indicated by red circle symbols) are generally higher than those of bulk RHEAs and the pure elements, while close to that of the TiZrNbHfTa films as reported by Cheng et al. [70]. By tunning the Ni content, the H/E value of the $TiZrNbHf_{1.6}Ni_x$ RHEA films varies from 0.043 to 0.059, and the H^3/E^2 value varies from 0.009 to 0.022. This finding indicates that the excellent mechanical properties of the $TiZrNbHf_{1.6}$ RHEA films can be effectively tailored by Ni addition, making the them promising materials as wear resistance coatings.

3.3. Deformation behaviors

The plastic deformation of the $TiZrNbHf_{1.6}Ni_x$ films was produced by the microindentaion tests (schematized in Fig. 10a) with a load of 500 mN, as presented in Fig. 10b–i. It can be seen from Fig. 10b that an obvious plastic pileup occurs around the indent in the crystal $TiZrNbHf_{1.6}$ film, indicating a homogeneous deformation. While the deformation mode varies in those films with different Ni content (Fig. 10c-i). First, profuse shear bands (in regular circle-shaped) can be observed around the indent with Ni content of 8.4 at.% ($x = 0.4$, Fig. 10c). At the same time, the corresponding pileup height (h_p) is increased as compared with the film without Ni content (Fig. 10j). Second, only plastic pileup occurs in the film with Ni content of 20.4 at.% ($x = 1.2$, Fig. 10d), which is close to the morphology observed in $TiZrNbHf_{1.6}$ film (Fig. 10b). This finding demonstrated that deformability of $TiZrNbHf_{1.6}Ni_{1.2}$ is superior to $TiZrNbHf_{1.6}Ni_{0.4}$ film, which can be attributed to the relatively soft nature of the former (5.2 GPa) than the later (5.9 GPa), as plotted in Fig. 10j. However, catastrophic cracks with a maximum crack width of ~ 660 nm, occur in the film with Ni content of 28.5 at.% ($x = 1.8$, Fig. 10e and f). No obvious plastic pileup can be detected around the indent (Fig. 10j), suggesting a significant brittleness behavior. It is clear that the crack initiates from the center of the indenter and propagates directly along the edge of the indenter (Fig. 10e and f), which is the typical radius crack [72]. As Ni content increases to 34.5 at.% ($x = 2.5$, Fig. 10g) and 38.5 at.% ($x = 3$, Fig. 10h), shear banding instead of cracks dominates the deformation and produces obvious pileups with a height of ~ 230 nm as measured by atomic force microscope (Fig. 10j), which is similar to the deformation as observed in $TiZrNbHf_{1.6}Ni_{0.4}$ film (Fig. 10c). With further increase Ni content to 50.8 at.% ($x = 4.6$), a slight pileup (~ 150 nm) and high-density nano-cracks (indicated by red arrows in Fig. 10i) can be observed around the indent. In contrast to the cracks observed in Fig. 10f, these nano-cracks are initially formed in the as-deposited $TiZrNbHf_{1.6}Ni_{4.6}$ film (Fig. 2f) and did not cause the film to fracture even subject to a large deformation imposed by microindentation, which suggests its excellent instinct toughness.

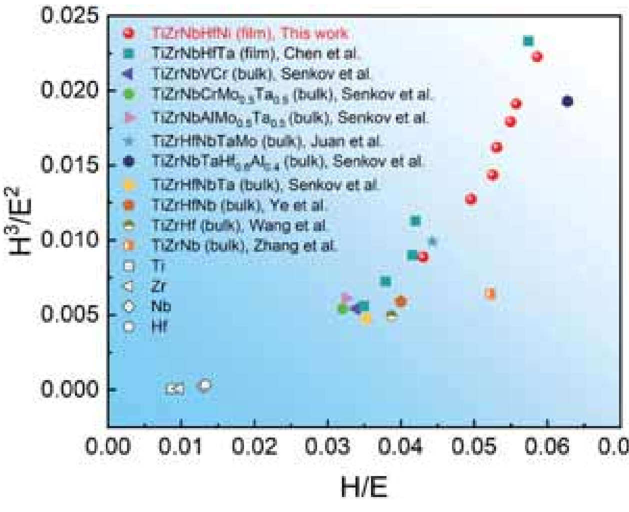

Fig. 9. Relationship between the H/E and H^3/E^2 of the designed $TiZrNbHf_{1.6}Ni_x$ RHEA films and other bulk RHEAs (TiZrHfNb [5], TiZrHfNbTa [20], $TiZrNbTaHf_{0.6}Al_{0.4}$ [25], TiZrHfNbTaMo [67], $TiZrNbAlMo_{0.5}Ta_{0.5}$ [25], $TiZrNbCrMo_{0.5}Ta_{0.5}$ [21], TiZrNbVCr [22], TiZrNb [68], TiZrHf [69]), HEA film (TiZrNbHfTa [70]) and pure metal elements (Ti, Zr, Nb, Hf) [20].

Based on the above nano and micro-indentation results, it is believed that $x = 1.8$ is a critical composition, in which the hardness reaches the maximum and the deformability is the poorest, i.e., obvious brittleness. When the Ni content is below or above 1.8, the hardness of the film is decreased while the deformability is elevated (as seen in Fig. 10). The hardness of metallic glasses is strongly determined by the chemical bonding (primarily metallic bonding) between the atoms, which can be broken and reformed at the atomic scale under the applied stress [73,74]. The addition of Ni element with a small atomic size compared with the base elements (Ti, Zr, Nb, Hf, Ni) may potentially enhance the bonds of the amorphous alloy, which leads to the maximum hardness achieved at $x = 1.8$. Besides, it is widely believed that the distribution of free volume controls the deformation of metallic glasses, and brittleness usually occurs when the free volume drops below a critical level required for inhomogeneous plastic flow [73]. However, the addition of heavy elements (usually with a density > 5 g/cm^3) improves the atomic packing of the metallic glasses, which lowers the free volume content of the amorphous alloy [74]. Hence, it is easy to envision that as the Ni (with a density of ~ 8.9 g/cm^3) composition is increased to a critical value, the free volume content of the $TiZrNbHf_{1.6}Ni_x$ amorphous alloy may be significantly reduced, resulting in the extreme limitation of atomic mobility, which may explain the brittleness deformation in $x = 1.8$. It should be pointed out that since all the Ni-doped samples have the same complex amorphous structure, it may be hard to detect a difference between $x = 1.8$ and other amorphous samples from the SEM, XRD and TEM analyses. Besides, the specific chemic bonding and the free volume can be influenced by the solubility of Ni atomic into the $TiZrNbHf_{1.6}$ alloy with the change of Ni content, which is difficult to determine in the current experimental study, further investigation by density functional theory combined with molecular dynamics calculation is needed in future work.

To further investigate the deformation mechanisms of the BCC-structured film without Ni addition and the Ni-doped amorphous films, the cross sections of micro-indents of $TiZrNbHf_{1.6}$ and $TiZrNbHf_{1.6}Ni_{0.4}$ alloy films were milled by FIB and characterized by TEM, as shown in Fig. 11 and Fig. 12. First, it can be seen that in $TiZrNbHf_{1.6}$ film the columnar grains deformed in a ductile yielding without cracks or voids formation (Fig. 11a). Moreover, the magnified HAADF-STEM image (Fig. 11b) shows that these grains undergo a large buckling deformation without fracture, which demonstrates its excellent plastic deformability, which is consistent with observed plastic pileup (Fig. 10b). In the region near the pileup region, the deformation is mainly accommodated by the intersqueezing of adjacent grains under the constraints of the indenter while the grain boundaries remain intact, as illustrated in Fig. 11c. A lot of defects (stacking faults and dislocations) are dectected in the deformed region as indicated in the inverse FFT image (Fig. 11e). Generally, there are no stable stacking faults in

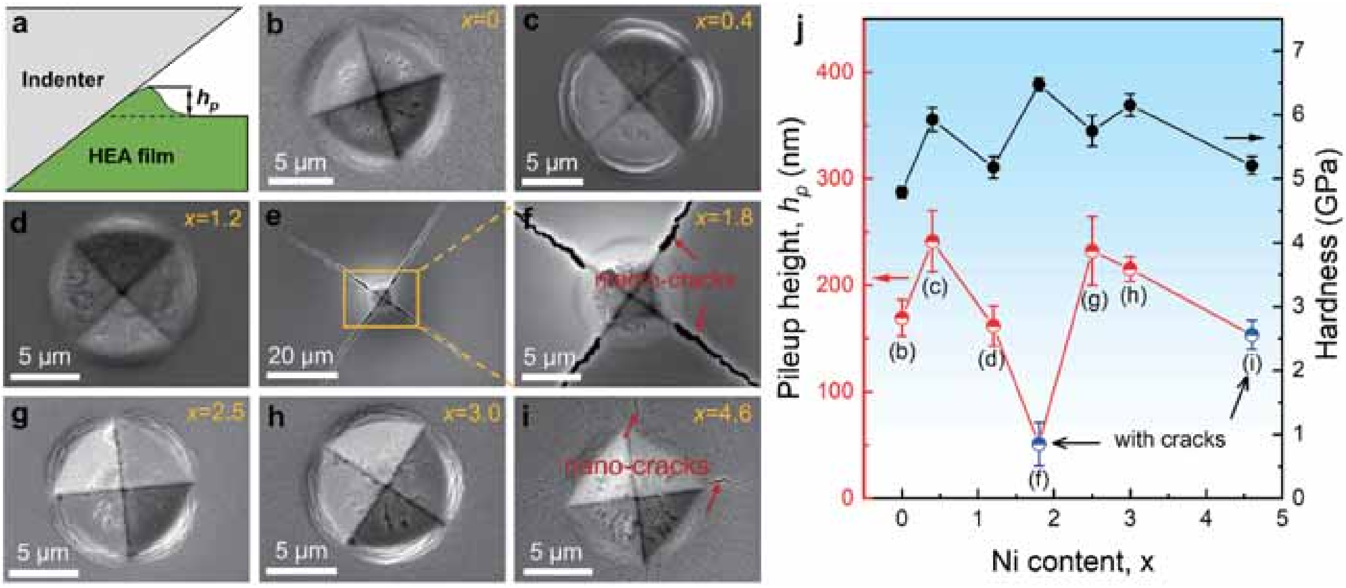

Fig. 10. Deformation of the TiZrNbHf$_{1.6}$Ni$_x$ (x = 0, 0.4, 1.2, 1.8, 2.5, 3.0, 4.6) RHEA films under microindentation with a load of 500 mN. (a) Illustration of the microindentation-induced deformation and corresponding plastic pileup height (h_p). (b–i) Residual morphology of the indents. (j) The pileup height h_p and the nanohardness with the variation of Ni content of the TiZrNbHf$_{1.6}$Ni$_x$ HEA films.

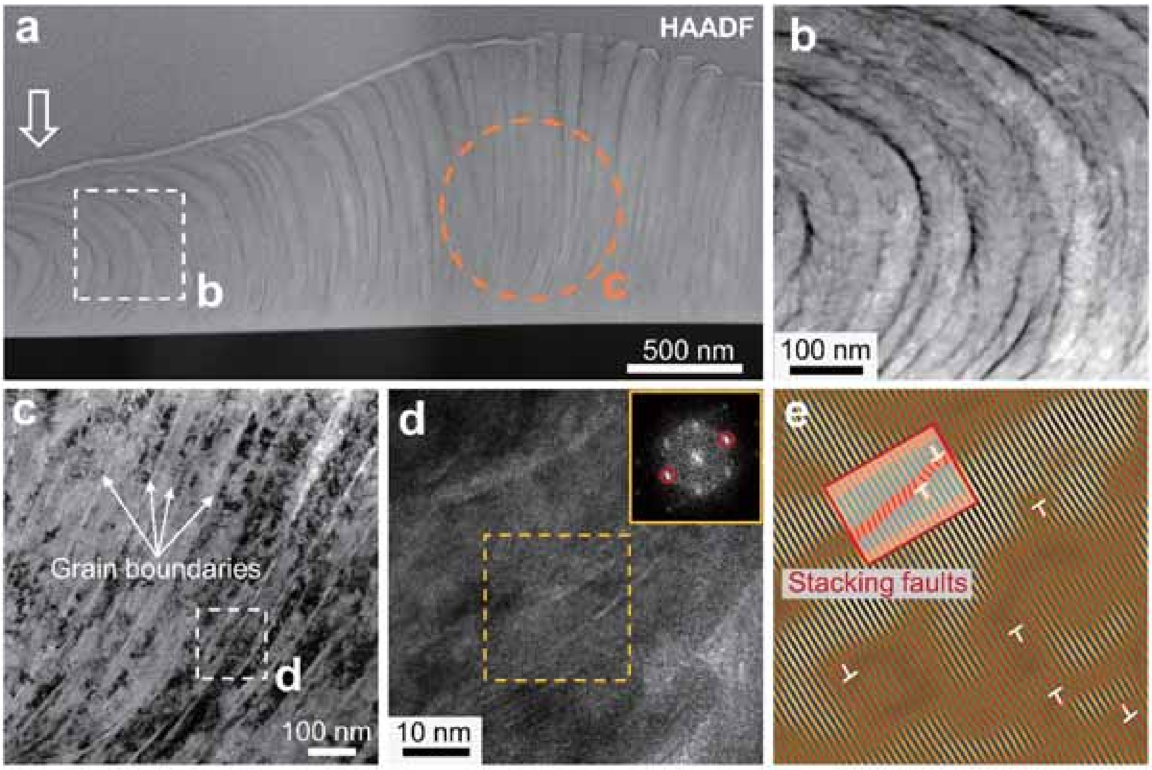

Fig. 11. Cross-sectional TEM micrographs of TiZrNbHf$_{1.6}$ HEA film after microindentation of 500 mN. (a) HAADF-STEM image. (b) The magnified region as indicated in (a). (c) Brigth-field TEM image taken from the region indicated in (a). (d) HRTEM micrograph of the area marked in (c), the inset is the FFT image of the orange box region. (e) Inverse FFT pattern obtained from the mask position (red dotted circle) indicated in the FFT image, showing the reserved stacking faults and dislocation ("⊥"). The white arrow in (a) designates the position of the indenter.

BCC metals and the deformation is mainly accommodated by the motion of screw dislocations with type Burgers vector $1/2 < 111 >$ [75]. Thus, the formation of a stacking fault may be originated from a dislocation dissociation reaction [76]:

$$a/2[11\bar{1}]\rightarrow a/6[11\bar{1}]+a/3[11\bar{1}] \quad (5)$$

The two partials in the right term can glide out of their original slip plane into other differently oriented {112} planes. This dislocation dissociation reaction results in an energy reduction of about 45% according to the Burgers vector square energy criterion [76]. Therefore, this dislocation dissociation is energetically favorable and might be responsible for the deformation stacking faults in the TiZrNbHf$_{1.6}$ RHEA

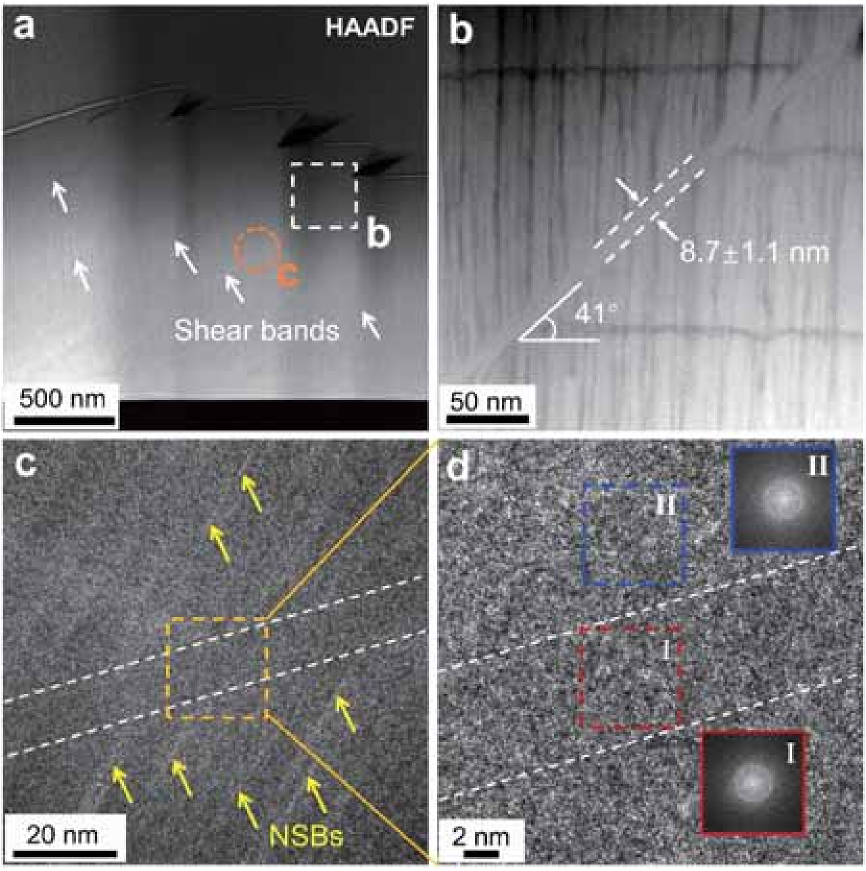

Fig. 12. Cross-sectional TEM observations of micro-indents for the TiZrNbHf$_{1.6}$Ni$_{0.4}$ film. (a) HAADF-STEM image of the shear banding region. (b) Magnified microstructural area indicated in (a). (c, d) HRTEM images of the shear banding region, the insets in (d) are the corresponding FFT patterns of the box regions marked in (d).

film with BCC structure.

Fig. 12a presents the cross-sectional HAADF-STEM image of the TiZrNbHf$_{1.6}$Ni$_{0.4}$ film after microindentation, showing the typical shear banding deformation (indicated by the white arrows) of the amorphous alloys. These shear bands are formed in a direction of 41° (close to 45°, at which angle the shear stress reaches the maximum) with respect to the substrate. The shear band width is measured to be 8.7 nm (Fig. 12b), which is in accordance with the typical shear band width (~ 10 nm) for many amorphous alloys [77]. Moreover, it can be noted that those NSBs (bright bands indicated by yellow arrows) can not be detected within the shear band due to the large shear deformation, whereas those NSBs outside the shear banding region remain intact (Fig. 12c). It can be speculated that the NSBs are sheared into the shear band and undergo a large shear displacement, resulting in rearranging of the local atom or STZs. Yu et al. [78] suggested that like the STZs, the NSBs generated by β relaxations contribute to the plasticity of amorphous alloys. Similarly, Chen et al. [42] demonstrated that the NSBs formed in NiW amorphous alloy film lead to significant hardening and toughening effects since they promote multiple shear banding under micropillar compression [42]. Thus, the pre-existing NSBs may be beneficial for the generation of multiple shear bands upon microindentation due to their high atomic motility, hence enhancing the deformability of HEA films. Although previous studies [42,79] indicated that β relaxation and subsequently shear banding deformation may cause crystallization within the shear band, no crystallization is detected in the present study inside the sheared region (region I, Fig. 12d) or near-sheared region (region II, Fig. 12d) (i.e., no crystal spots be detected in the FFT images). This may be attributed to the distinguished atomic configuration and thermal activation conditions for crystallization in different amorphous systems [79].

4. Concluding remarks

In summary, TiZrNbHf$_{1.6}$Ni$_x$ (x = 0, 0.4, 1.2, 1.8, 2.5, 3.0, 4.6) HEA films were prepared by the co-sputtering method using the pure metal targets, and the effect of Ni content on the microstructure and mechanical behavior of the films were systematically investigated. The main findings are concluded in the following.

A transition from a single BCC to an amorphous structure was observed in the HEA films when Ni content increased to 0.4, as confirmed by XRD and TEM. The phase structure of the HEA films with different Ni content is satisfied with the theoretical prediction of the published criteria for those bulk HEAs based on the calculated thermodynamic parameters δ, Ω and ΔH_{mix}.

A significant hardness increase (8–35%) is achieved via Ni addition, i.e., increased from 4.8 GPa without Ni addition to 5.2–6.5 GPa with Ni-doped HEA films. Additionally, the mechanical property of the TiZrNbHf$_{1.6}$Ni$_x$ films evaluated by hardness (H) and elastic modulus (E) with H/E and H^3/E^2 is superior to the bulk TiZrNb, TiZrNbHf, TiZrNbHfTa and their derived alloys (e.g., TiZrNbVCr, TiZrNbHfTaAl$_x$, TiZrNbHfTaMo$_x$), suggesting them a promising material for wear resistance coatings.

Microindentation tests revealed three deformation modes in the HEA films with different Ni compositions. A slight plastic pileup occurred in the films with Ni content of 1.2 and 4.6, while brittleness fracture induced by cracks was observed in the film with the Ni content of 1.8, and shear banding prevailed in the films with Ni content of 0.4, 2.5 and 3.0.

The present work provides a paragon for designing HEA films with amorphous structure and high hardness by appropriate element addition, which may guide the development of HEA coatings with high wear and corrosion resistance.

CRediT authorship contribution statement

Qin Feng: Investigation, Methodology, Visualization, Formal analysis, Writing – original draft. **Dai Kaiqing:** Investigation. **Chen Shaohua:** Writing – review & editing. **Li Jianjun:** Conceptualization, Resources, Project administration, Supervision, Funding acquisition, Writing – review & editing.

Declaration of Competing Interest

The authors declare that they have no known competing financial interests or personal relationships that could have appeared to influence the work reported in this paper.

Data Availability

All data generated or analyzed during this study are included in this published article, or are available from the corresponding authors on reasonable request.

Acknowledgments

The authors appreciate the financial supports from National Natural Science Foundation of China (NSFC) (Grant No. 12272413) and the Department of Science and Technology of Hunan Province, China (Grant No. 2021RC3022).

References

[1] Z. Li, K.G. Pradeep, Y. Deng, D. Raabe, C.C. Tasan, Metastable high-entropy dual-phase alloys overcome the strength-ductility trade-off, Nature 534 (2016) 227–230.

[2] G. Laplanche, A. Kostka, O.M. Horst, G. Eggeler, E.P. George, Microstructure evolution and critical stress for twinning in the CrMnFeCoNi high-entropy alloy, Acta Mater. 118 (2016) 152–163.

[3] F. Otto, A. Dlouhý, C. Somsen, H. Bei, G. Eggeler, E.P. George, The influences of temperature and microstructure on the tensile properties of a CoCrFeMnNi high-entropy alloy, Acta Mater. 61 (2013) 5743–5755.

[4] B. Gludovatz, A. Hohenwarter, D. Catoor, E.H. Chang, E.P. George, R.O. Ritchie, A fracture-resistant high-entropy alloy for cryogenic applications, Science 345 (2014) 1153–1158.

[5] Y.X. Ye, C.Z. Liu, H. Wang, T.G. Nieh, Friction and wear behavior of a single-phase equiatomic TiZrHfNb high-entropy alloy studied using a nanoscratch technique, Acta Mater. 147 (2018) 78–89.

[6] E.P. George, D. Raabe, R.O. Ritchie, High-entropy alloys, Nat. Rev. Mater. 4 (2019) 515–534.

[7] J.W. Yeh, S.K. Chen, S.J. Lin, J.Y. Gan, T.S. Chin, T.T. Shun, C.H. Tsau, S.Y. Chang, Nanostructured high-entropy alloys with multiple principal elements: novel alloy design concepts and outcomes, Adv. Eng. Mater. 6 (2004) 299–303.

[8] B. Cantor, I.T.H. Chang, P. Knight, A.J.B. Vincent, Microstructural development in equiatomic multicomponent alloys, Mater. Sci. Eng. A 375 (2004) 213–218.

[9] Y. Zhang, T.T. Zuo, Z. Tang, M.C. Gao, K.A. Dahmen, P.K. Liaw, Z.P. Lu, Microstructures and properties of high-entropy alloys, Prog. Mater. Sci. 61 (2014) 1–93.

[10] F. Otto, A. Dlouhy, C. Somsen, H. Bei, G. Eggeler, E.P. George, The influences of temperature and microstructure on the tensile properties of a CoCrFeMnNi high-entropy alloy, Acta Mater. 61 (2013) 5743–5755.

[11] Z. Wu, H. Bei, G.M. Pharr, E.P. George, Temperature dependence of the mechanical properties of equiatomic solid solution alloys with face-centered cubic crystal structures, Acta Mater. 81 (2014) 428–441.

[12] Y.J. Zhou, Y. Zhang, Y.L. Wang, G.L. Chen, Solid solution alloys of AlCoCrFeNiTix with excellent room-temperature mechanical properties, Appl. Phys. Lett. 90 (2007), 181904.

[13] F.J. Wang, Y. Zhang, Effect of Co addition on crystal structure and mechanical properties of Ti0.5CrFeNiAlCo high entropy alloy, Mater. Sci. Eng. A 496 (2008) 214–216.

[14] A. Gali, E.P. George, Tensile properties of high- and medium-entropy alloys, Intermetallics 39 (2013) 74–78.

[15] O.N. Senkov, G.B. Wilks, D.B. Miracle, C.P. Chuang, P.K. Liaw, Refractory high-entropy alloys, Intermetallics 18 (2010) 1758–1765.

[16] O.N. Senkov, G.B. Wilks, J.M. Scott, D.B. Miracle, Mechanical properties of Nb25Mo25Ta25W25 and V20Nb20Mo20Ta20W20 refractory high entropy alloys, Intermetallics 19 (2011) 698–706.

[17] O.N. Senkov, D.B. Miracle, K.J. Chaput, J.-P. Couzinie, Development and exploration of refractory high entropy alloys—a review, J. Mater. Res. 33 (2018) 3092–3128.

[18] F. Habashi, Historical introduction to refractory metals, Miner. Process. Extr. Metall. Rev. 22 (2001) 25–53.

[19] D.B. Miracle, O.N. Senkov, A critical review of high entropy alloys and related concepts, Acta Mater. 122 (2017) 448–511.

[20] O.N. Senkov, J.M. Scott, S.V. Senkova, D.B. Miracle, C.F. Woodward, Microstructure and room temperature properties of a high-entropy TaNbHfZrTi alloy, J. Alloy. Compd. 509 (2011) 6043–6048.

[21] O.N. Senkov, C.F. Woodward, Microstructure and properties of a refractory NbCrMo0.5Ta0.5TiZr alloy, Mater. Sci. Eng. A 529 (2011) 311–320.

[22] O.N. Senkov, S.V. Senkova, D.B. Miracle, C. Woodward, Mechanical properties of low-density, refractory multi-principal element alloys of the Cr–Nb–Ti–V–Zr system, Mater. Sci. Eng. A 565 (2013) 51–62.

[23] N.N. Guo, L. Wang, L.S. Luo, X.Z. Li, Y.Q. Su, J.J. Guo, H.Z. Fu, Microstructure and mechanical properties of refractory MoNbHfZrTi high-entropy alloy, Mater. Des. 81 (2015) 87–94.

[24] Y.D. Wu, Y.H. Cai, T. Wang, J.J. Si, J. Zhu, Y.D. Wang, X.D. Hui, A refractory Hf25Nb25Ti25Zr25 high-entropy alloy with excellent structural stability and tensile properties, Mater. Lett. 130 (2014) 277–280.

[25] O.N. Senkov, S.V. Senkova, C. Woodward, Effect of aluminum on the microstructure and properties of two refractory high-entropy alloys, Acta Mater. 68 (2014) 214–228.

[26] M. Srikanth, A.R. Annamalai, A. Muthuchamy, C.-P. Jen, A review of the latest developments in the field of refractory high-entropy alloys, Crystals (2021).

[27] O.N. Senkov, S. Rao, K.J. Chaput, C. Woodward, Compositional effect on microstructure and properties of NbTiZr-based complex concentrated alloys, Acta Mater. 151 (2018) 201–215.

[28] A. Liu, Y. Jing, X. Cui, Q. Ding, Y. Song, G. Jin, Influence of atomic size effect on the properties of high entropy alloy coatings, Mater. Today Commun. 37 (2023), 107150.

[29] B.R. Braeckman, F. Misják, G. Radnóczi, D. Depla, The influence of Ge and In addition on the phase formation of CoCrCuFeNi high-entropy alloy thin films, Thin Solid Films 616 (2016) 703–710.

[30] Y.C. Hsu, C.L. Li, C.H. Hsueh, Modifications of microstructures and mechanical properties of CoCrFeMnNi high entropy alloy films by adding Ti element, Surf. Coat. Tech. 399 (2020), 126149.

[31] S. Fang, C. Wang, C.L. Li, J.H. Luan, Z.B. Jiao, C.T. Liu, C.H. Hsueh, Microstructures and mechanical properties of CoCrFeMnNiVx high entropy alloy films, J. Alloy. Compd. 820 (2020), 153388.

[32] Y.H. Liang, C.L. Li, C.H. Hsueh, Effects of Nb addition on microstructures and mechanical properties of Nbx-CoCrFeMnNi high entropy alloy films, Coatings 11 (2021) 1539.

[33] S.S. Sohn, A. Kwiatkowski da Silva, Y. Ikeda, F. Körmann, W. Lu, W.S. Choi, B. Gault, D. Ponge, J. Neugebauer, D. Raabe, Ultrastrong medium-entropy single-phase alloys designed via severe lattice distortion, Adv. Mater. 31 (2019) 1807142.

[34] Q. Wei, A. Zhang, J. Han, B. Xin, B. Su, X. Wang, J. Meng, A novel Hf30Nb25Ta25Ti15Mo5 refractory high entropy alloy with excellent combination of strength and ductility, Mater. Sci. Eng. A 857 (2022), 144035.

[35] Z. Wang, C. Wang, Y.L. Zhao, Y.C. Hsu, C.L. Li, J.J. Kai, C.T. Liu, C.H. Hsueh, High hardness and fatigue resistance of CoCrFeMnNi high entropy alloy films with ultrahigh-density nanotwins, Int. J. Plast. 131 (2020), 102726.

[36] W.C. Oliver, G.M. Pharr, An improved technique for determining hardness and elastic modulus using load and displacement sensing indentation experiments, J. Mater. Res. 7 (1992) 1564–1583.

[37] Y. Li, J. Ma, P.K. Liaw, Y. Zhang, Exploring the amorphous phase formation and properties of W-Ta-(Cr, Fe, Ni) high-entropy alloy gradient films via a high-throughput technique, J. Alloy. Compd. 913 (2022), 165294.

[38] M. Abboud, A. Motallebzadeh, Ö. Duygulu, R. Maaß, S. Özerinç, Microstructure and nanomechanical behavior of sputtered CuNb thin films, Intermetallics 136 (2021), 107249.

[39] J. Wang, X. Liu, Y. Zhang, W. Cai, L. Wang, L. Tang, Effect of substrate bias on the microstructure and mechanical and tribological properties of ZrNbTiMo refractory high entropy alloy film, Surf. Coat. Tech. 455 (2023), 129214.

[40] Q. Wang, S.T. Zhang, Y. Yang, Y.D. Dong, C.T. Liu, J. Lu, Unusual fast secondary relaxation in metallic glass, Nat. Commun. 6 (2015) 7876.

[41] Y.H. Liu, T. Fujita, D.P.B. Aji, M. Matsuura, M.W. Chen, Structural origins of Johari-Goldstein relaxation in a metallic glass, Nat. Commun. 5 (2014) 3238.

[42] Z.Q. Chen, M.C. Li, X. Tong, Y. Zhao, J.Y. Xie, S.W. Guo, P. Huang, F. Wang, H. B. Ke, B.A. Sun, W.H. Wang, Hardening and toughening effects of intermediate nanosized structures in a confined amorphous alloy film, J. Mater. Sci. Technol. 118 (2022) 44–53.

[43] Y.Q. Wang, J.Y. Zhang, X.Q. Liang, K. Wu, G. Liu, J. Sun, Size- and constituent-dependent deformation mechanisms and strain rate sensitivity in nanolaminated crystalline Cu/amorphous Cu–Zr films, Acta Mater. 95 (2015) 132–144.

[44] X.D. Wang, T.D. Xu, Y. Su, Y. Tang, M. Sprung, Q.P. Cao, D.X. Zhang, J.Z. Jiang, Atomic dynamics transition in a Cu-Zr-Al metallic glass, Scr. Mater. 186 (2020) 268–271.

[45] Y. Zhang, Y.J. Zhou, J.P. Lin, G.L. Chen, P.K. Liaw, Solid-solution phase formation rules for multi-component alloys, Adv. Eng. Mater. 10 (2008) 534–538.

[46] X. Yang, Y. Zhang, Prediction of high-entropy stabilized solid-solution in multi-component alloys, Mater. Chem. Phys. 132 (2012) 233–238.

[47] S. Guo, C.T. Liu, Phase stability in high entropy alloys: formation of solid-solution phase or amorphous phase, Prog. Nat. Sci.: Mater. Int. 21 (2011) 433–446.

[48] S. Guo, Q. Hu, C. Ng, C.T. Liu, More than entropy in high-entropy alloys: forming solid solutions or amorphous phase, Intermetallics 41 (2013) 96–103.

[49] A. Takeuchi, A. Inoue, Quantitative evaluation of critical cooling rate for metallic glasses, Mater. Sci. Eng. A 304-306 (2001) 446–451.

[50] A. Takeuchi, A. Inoue, Classification of bulk metallic glasses by atomic size difference, heat of mixing and period of constituent elements and its application to characterization of the main alloying element, Mater. Trans. 46 (2005) 2817–2829.

[51] J. Basu, B.S. Murty, S. Ranganathan, Glass forming ability: Miedema approach to (Zr, Ti, Hf)–(Cu, Ni) binary and ternary alloys, J. Alloy. Compd. 465 (2008) 163–172.

[52] J.Y. Zhang, X. Zhang, R.H. Wang, S.Y. Lei, P. Zhang, J.J. Niu, G. Liu, G.J. Zhang, J. Sun, Length-scale-dependent deformation and fracture behavior of Cu/X (X=Nb, Zr) multilayers: The constraining effects of the ductile phase on the brittle phase, Acta Mater. 59 (2011) 7368–7379.

[53] Z.P. Lu, H. Tan, S.C. Ng, Y. Li, The correlation between reduced glass transition temperature and glass forming ability of bulk metallic glasses, Scr. Mater. 42 (2000) 667–673.

[54] T.A. Waniuk, J. Schroers, W.L. Johnson, Critical cooling rate and thermal stability of Zr–Ti–Cu–Ni–Be alloys, Appl. Phys. Lett. 78 (2001) 1213–1215.

[55] J.M. Park, Y.C. Kim, W.T. Kim, D.H. Kim, Ti-based bulk metallic glasses with high specific strength, Mater. Trans. 45 (2004) 595–598.

[56] M. Xia, H. Zheng, J. Liu, C. Ma, J. Li, Thermal stability and glass-forming ability of new Ti-based bulk metallic glasses, J. Non-Cryst. Solids 351 (2005) 3747–3751.

[57] C.C. Tung, J.W. Yeh, T. Shun, S.K. Chen, Y.S. Huang, H.C. Chen, On the elemental effect of AlCoCrCuFeNi high-entropy alloy system, Mater. Lett. 61 (2007) 1–5.

[58] H.P. Chou, Y.S. Chang, S.K. Chen, J.W. Yeh, Microstructure, thermophysical and electrical properties in AlxCoCrFeNi (0≤x≤2) high-entropy alloys, Mater. Sci. Eng. B 163 (2009) 184–189.

[59] K.C. Hsieh, C.F. Yu, W.T. Hsieh, W.R. Chiang, J.S. Ku, J.H. Lai, C.P. Tu, C.C. Yang, The microstructure and phase equilibrium of new high performance high-entropy alloys, J. Alloy. Compd. 483 (2009) 209–212.

[60] F.J. Wang, Y. Zhang, G.L. Chen, Atomic packing efficiency and phase transition in a high entropy alloy, J. Alloy. Compd. 478 (2009) 321–324.

[61] B. Ren, Z.X. Liu, D.M. Li, L. Shi, B. Cai, M.X. Wang, Effect of elemental interaction on microstructure of CuCrFeNiMn high entropy alloy system, J. Alloy. Compd. 493 (2010) 148–153.

[62] Y. Xiao, X. Peng, T. Fu, L21-strengthened body-centered-cubic high-entropy alloy with excellent mechanical properties, Intermetallics 145 (2022), 107539.

[63] J. Liu, Y. Huang, W. Liu, Y. Wang, Y. Zhang, Y. Ma, Effect of tantalum concentration on the microstructure and mechanical properties of novel W–Ta-Re alloy, Vacuum 207 (2023), 111627.

[64] Y. Wang, Z. Wang, A. Hobhaydar, Z. Qiu, B. Dong, Q. Gu, Z. Pan, D. Wexler, H. Zhu, X. Chen, M. Zhang, H. Li, Tungsten doping enhances the mechanical properties of FeCr2V-based medium entropy alloy revealed by experiments and calculations, J. Alloy. Compd. 940 (2023), 168861.

[65] R. Saha, W.D. Nix, Effects of the substrate on the determination of thin film mechanical properties by nanoindentation, Acta Mater. 50 (2002) 23–38.

[66] A. Leyland, A. Matthews, On the significance of the H/E ratio in wear control: a nanocomposite coating approach to optimised tribological behaviour, Wear 246 (2000) 1–11.

[67] C.C. Juan, M.H. Tsai, C.W. Tsai, C.M. Lin, W.R. Wang, C.C. Yang, S.K. Chen, S. J. Lin, J.W. Yeh, Enhanced mechanical properties of HfMoTaTiZr and HfMoNbTaTiZr refractory high-entropy alloys, Intermetallics 62 (2015) 76–83.

[68] Y. Zhang, W.J. Peng, Microstructural control and properties optimization of high-entrop alloys, Procedia Eng. 27 (2012) 1169–1178.

[69] S. Wang, D. Wu, H. She, M. Wu, D. Shu, A. Dong, H. Lai, B. Sun, Design of high-ductile medium entropy alloys for dental implants, Mater. Sci. Eng. C. 113 (2020), 110959.

[70] C. Cheng, X. Zhang, M.J.R. Haché, Y. Zou, Magnetron co-sputtering synthesis and nanoindentation studies of nanocrystalline (TiZrHf)x(NbTa)1−x high-entropy alloy thin films, Nano Res. 15 (2021) 4873–4879.

[71] P.H. Mayrhofer, C. Mitterer, J. Musil, Structure–property relationships in single- and dual-phase nanocrystalline hard coatings, Surf. Coat. Tech. 174-175 (2003) 725–731.

[72] S. Zhang, X. Zhang, Toughness evaluation of hard coatings and thin films, Thin Solid Films 520 (2012) 2375–2389.

[73] C. Schuh, T. Hufnagel, U. Ramamurty, Mechanical behavior of amorphous alloys, Acta Mater. 55 (2007) 4067–4109.

[74] T. Rouxel, J.-i Jang, U. Ramamurty, Indentation of glasses, Prog. Mater. Sci. 121 (2021), 100834.

[75] W. Cai, V.V. Bulatov, J. Chang, J. Li, S. Yip, Dislocation core effects on mobility, Dislocations Solids 12 (2004).

[76] J.S. Hirschhorn, Stacking faults in the refractory metals and alloys — a review, J. Less-Common Met. 5 (1963) 493–509.

[77] Y. Zhang, A.L. Greer, Thickness of shear bands in metallic glasses, Appl. Phys. Lett. 89 (2006), 071907.

[78] H.B. Yu, W.H. Wang, K. Samwer, The β relaxation in metallic glasses: an overview, Mater. Today 16 (2013) 183–191.

[79] W.H. Wang, Dynamic relaxations and relaxation-property relationships in metallic glasses, Prog. Mater. Sci. 106 (2019), 100561.